Applied Catalysis B: Environmental 241 (2019): 375-384

**DOI:** https://doi.org/10.1016/j.apcatb.2018.09.070

# NATURE AND PHOTOREACTIVITY OF $TiO_2$-rGO NANOCOMPOSITES IN AQUEOUS SUSPENSIONS UNDER UV-A IRRADIATION

A.Tolosana-Moranchel[1*], J. A. Casas[1], A. Bahamonde[2], L. Pascual[2], L. I. Granone[3,4], J. Schneider[3,4], R. Dillert[3,4], D. W. Bahnemann[3,4,5]

[1]Sección de Ingeniería Química, Facultad de Ciencias, C/ Francisco Tomás y Valiente 7, Universidad Autónoma de Madrid, 28049 Madrid (Spain).

[2]Instituto de Catálisis y Petroleoquímica, ICP-CSIC, C/ Marie Curie 2, 28049 Madrid (Spain).

[3]Institute of Technical Chemistry, Gottfried Wilhelm Leibniz University Hannover, Callinstr. 5, 30167 Hannover, Germany.

[4]Laboratorium für Nano- und Quantenengineering, Gottfried Wilhelm Leibniz Universität Hannover, Schneiderberg 39, 30167 Hannover, Germany.

[5]Laboratory of Photoactive Nanocomposite Materials, Department of Photonics, Faculty of Physics, Saint-Petersburg State University, Ulianovskaia str. 3, Peterhof, Saint-Petersburg 198504, Russian Federation.

## ABSTRACT

Different studies to unravel the nature of the activity of $TiO_2$ photocatalysts modified with rGO were carried out. The band edge potentials and the band gap energy of the nanocomposites were determined by performing electrochemical impedance and UV-vis diffuse reflectance measurements, respectively. However, no changes were observed when $TiO_2$ is modified with rGO. Nevertheless, the presence of rGO in the hybrid composite led to a low charge transfer resistance across the electrode-electrolyte interface, observing even a tenfold increase in the photocurrent values in methanol photo-oxidation for P25-rGO 1%. Moreover, a higher oxygen reduction current was found when increasing the rGO concentration that could lead to a higher ROS formation. In order to analyze the beneficial properties of the hybrid materials, the influence of rGO doping ratio on oxalic acid photocatalytic degradation and on oxalic acid adsorption onto the nanocomposites surface was studied, both of them under UV-A light irradiation. In addition, the photoactivity of the conduction band electrons and the valence band holes was investigated by performing EPR and transient absorption spectroscopy measurements under UV-A illumination in $O_2$ or $N_2$ atmospheres. It was demonstrated that rGO behaved as an electron acceptor. Finally, TAS results under $O_2$ and $N_2$ atmospheres proved that the role played by rGO was not as crucial in excess of dissolved $O_2$ as in $N_2$ atmosphere. These findings agree with the observed photocatalytic activity and EPR measurements. Nevertheless, generation of $HO^{\bullet}$ in $N_2$ saturated suspensions was highly increased with the addition of rGO.

*Keywords:* $TiO_2$-rGO, reduced graphene oxide, oxalic acid, mechanism, ATR-FTIR

*Corresponding author, e-mail address: alvaro.tolosana@uam.es

## 1. INTRODUCTION

Photocatalytic Advanced Oxidation Process (AOP) based on semiconductors have emerged as a promising technology for water treatment [1]. The increasing interest is related to the ability of semiconductors to generate reactive electron-hole pairs when illuminated with light of energy greater than their band gap. These photogenerated charge carriers are able to form highly reactive chemical species, such as hydroxyl radicals $HO^{\bullet}$, which allow disinfecting water and/or degrading highly recalcitrant pollutants present in aqueous systems [2-4].

Because of the high band gap value and the low photonic efficiency exhibited by $TiO_2$, a great deal of attention has been focused on the synthesis of new hybrid materials lacking these limitations [5-8]. Graphene- and graphene-derivative-based $TiO_2$ have been proposed as highly photoactive nanocomposites due to their unique properties, such as large specific surface area and high electrical conductivity [9-14]. Furthermore, the photoactivity is enhanced on account on the fact that graphene oxide (GO) and reduced graphene oxide (rGO) absorb light in the UV-Vis wavelength region, leading to the formation of reactive oxygen species [2, 12, 13].

Unfortunately, no consensus has been completely stablished so far about the role of rGO during the photocatalytic treatment of pollutants dissolved in water. Minella et al. [15] proposed a mechanism of underlying reactions in the presence of $TiO_2$-rGO composites. The role played by rGO appears to depend on the adsorption and the light absorption properties of the substrate. Thus, only when the adsorption of the organic probe compound is significant, the electron transfer from the two phases can occur. This evinces the necessity to deepen into the understanding of the underlying mechanism. However, to evaluate the right development of the photocatalysts and the influence of their improved properties on the photocatalytic activity, the knowledge of the energetic position of the conduction and valence band edges and the reaction mechanism itself is crucial.

In this study, the nature of the activity of a $TiO_2$ photocatalyst modified with rGO synthesized by a hydrothermal method was investigated. Different rGO doping ratios were analyzed in the photodegradation of oxalic acid under UV-A light irradiation. In order to obtain a better knowledge about the origin and mechanism of the observed photoactivity, oxalic acid photodegradation runs were carried out. The actual position of the band edges and the band gap energy were determined by performing electrochemical impedance spectroscopy and UV-vis diffuse reflectance, respectively. Furthermore, electrochemical impedance spectroscopy and photocurrent response measurements were carried out to study the charge separation of the photo-generated charge carriers. Additionally, the reduction pathways of oxygen were investigated by measuring the oxygen reduction current at different potentials. Finally, EPR and transient absorption spectroscopy (TAS) experiments were

performed to investigate the conduction band electrons and the valence band holes activity under UV-A illumination under $O_2$ or $N_2$ atmospheres. These results were related to the performance observed in the oxalic acid oxidation reactions.

## 2. EXPERIMENTAL SECTION

### *2.1 Materials*

Graphene oxide (GO) water dispersions (0.4 wt% Concentration) were purchased from Graphenea company. The GO used had a monolayer content over 95%, a particle size of 600 nm (DSL) and the following elemental analysis data was obtained: C=49–56%, H=0–1%, N=0–1%, S=2–4%, O=41–50%. Titanium dioxide P25 Aeroxide® (80:20 anatase-rutile, BET specific surface area 54 $m^2/g$, average anatase and rutile crystal size of 21 and 33 nm, respectively) was provided by Evonik Company. The spin trap 5,5-dimethyl-1-pyrroline-N-oxide (DMPO), oxalic acid (OA) (≥ 99%), FTO (fluorine-doped tin oxide SnO2:F) glass and Dimethyl Sulfoxide (DMSO) were purchased from Sigma-Aldrich.

Deionized water ($H_2O$) was supplied from a Millipore Milli-Q system with a resistivity equal to 18.2 MΩ·cm. pH adjustments and measurements were performed using KOH provided by PanReac AppliChem. All the chemicals were used as received without further purification.

### *2.2 Synthesis of P25-rGO*

P25-rGO composites were prepared by a hydrothermal method. To sum up, 2 g of P25 were suspended in 400 mL of deionized water and dispersed for 1 hour using a 100 MHz tip (Misonix Microson 2000XL). Subsequently, the desired amount of GO was added to the suspension and sonicated for another hour to achieve a good dispersion of GO sheets in a homogenous medium. Subsequent to sonication, the mixture was transferred to a 600-mL Teflon-lined stainless steel autoclave reactor and subjected to hydrothermal treatment overnight at 120 ºC. After that, the composite was collected by centrifugation and dried at 60 ºC. The weight ratio P25: rGO was 0, 0.1, 0.5 and 1%, called along the paper as P25-rGO 0%, P25-rGO 0.1%, P25-rGO 0.5% and P25-rGO 1%, respectively.

### *2.3 Photocatalyst characterization*

Diffuse reflectance spectra were recorded with a UV-Visible Varian, Cary 100 Bio UV-Vis, equipped with an integrating sphere. Analyses of the band gap transitions of the samples were made using the Kubelka-Munk radiative transfer model and the Tauc plots [16]. An indirect allowed transition was considered to calculate the band gap energies [17, 18]. Raman spectrum was recorded on a Renishaw Micro Raman spectrometer (λ = 532 nm) equipped with a 20 mW He-Ne laser emitting at 532 nm. The spectra were recorded using 0.2mW of incident power, 5 repetitions and 10 seconds of acquisition time.

Catalysts structural characterization were performed with a X-ray polycrystal PANalytical X´Pert PRO using nickel-filtered Cu Kα (1.541874 Å) radiation operating at 40 kV and 40 mA,

with a 0.02° step size and accumulating a total of 50 s per point. Crystallite sizes was estimated by employing the Scherrer equation [19] and the crystalline phases were identified by comparison with ICDD PDF database [20]. The quantification of each previously selected crystalline phase was automatically calculated by X'Pert Highscore Plus software by the RIR (Reference Intensity Ratio) method.

Scanning electron microscopy (SEM) analyses were performed to determine morphology of the studied $TiO_2$ powders (Philips XL 30 S-FEG). Transmission Electron Microscope study of the composites was carried out in a field emission gun JEOL 2100F microscope operating at 200KV. Specimens for Transmission electron microscopy were prepared by dry deposition of the composites in a lacey carbon copper grid.

Transient absorption spectroscopy (TAS), described previously in more detail [21], was carried out using an Applied Photophysics LKS 80 Laser Flash Photolysis Spectrometer. The proper diffuse reflectance accessory was used to measure in diffuse reflectance mode. The samples were excited by an Nd-YAG laser (Quantel; Brilliant B; 3rd harmonic, 355 nm) and light up by a pulsed xenon lamp (Osram XBO; 150 W) to analyze light absorption of the photogenerated transient species. Afterwards, the diffusely reflected light was led to the monochromator and detector (Hamamatsu PMT R928). For all the experiments excitations energy densities of 2.2 mJ $cm^{-2}$ per pulse were used, monitored by a Maestro energy meter (Gentec-EO). A 100 Ω value was always used as terminal resistance and the number of averages was 12 shots. All the samples were dry powder placed into a quartz flat cuvette and they were flushed with nitrogen or oxygen for more than 30 minutes before performing the measurements. To analyze the results obtained, the reflectance changes $\Delta J$ of the samples were obtained from the absorbance:

$$\Delta J = 1 - 10 \qquad \text{——}$$

Where $\Delta J$ can be correlated with the transient absorption of the photogenerated species and $\mathrm{I}$ and $\mathrm{I}$ are the intensities of the reflected light before and after the laser pulse, respectively.

*2.4 Electrochemical Characterization*

The photo-anodes of the synthesized photocatalysts were prepared by following the screen-printing method [22]. The detailed procedure is described in detail in the Supplementary Information: Procedure to prepare the photo-anodes by the screen-printing method.

The measurements were carried out with a three compartment cell consisting of a working (photo-) electrode (WE), a Pt wire counter electrode (CE) and an Ag/AgCl/KCl (3 M) reference electrode (RE). All potential values presented herein are pH-corrected and expressed vs. RHE (reversible hydrogen electrode). The photo-response of the prepared films was tested under chopped light irradiation at a constant potential 0.8 V vs. RHE by a Zennium potentiostat and a PECC-2 photoelectrochemical cell (Zahner-Elektrik GmbH & Co. KG). The illumination source, a 300 W Xe lamp with an AM 1.5-global filter providing an

intensity of 680 $W \cdot m^{-2}$ in the regime of 280–1000 nm (LOT-Quantum Design GmbH), was chopped on and off with a frequency of 300 mHz. Regarding the electrolyte, a 0.1 M $Na_2SO_4$ aqueous solution with 10% v/v $CH_3OH$ was used.

For the rest of electrochemical experiments a 0.1 M $Na_2SO_4$ aqueous solution was used as the electrolyte. The electrochemical impedance spectroscopies (EIS) of the as-prepared samples were carried out within a frequency range from 0.1 Hz to 30000 Hz and the applied bias was -0.0 V vs. RHE. The flat-band potentials ($V_{fb}$) were determined from Mott–Schottky plots by Impedance spectra collected in the potential range of +1 to 0.2 V vs. RHE with a step width of -25 mV. Each spectrum was recorded at a fixed potential in the frequency range of 0.1 to 30000 Hz with 10 steps per decade. A Randles circuit was used to fit the spectra to obtain the value of the space charge layer capacitance ($C_{SC}$) at each potential. Rather than ordinary capacitance, constant phase elements (CPE) were used. In this work the flat-band potentials of the photo-anodes were calculated from the resulting Mott–Schottky plots ($C^{-2}$ vs. applied potential). The extrapolation of the linear trend in the Mott–Schottky plot to the x-axis (potential) enables to calculate the $V_{fb}$ for a given semiconductor oxide [8, 16].

Oxygen reduction currents were obtained by performing linear sweep voltammetry both in nitrogen or oxygen-saturated electrolytic solutions in +0.8 V to -0.1 V potential range vs. RHE with a step width of 10 mV and a scan rate of 1 $mV \cdot s^{-1}$. The difference between both scans constitutes the oxygen reduction current.

*2.5 ATR-FTIR adsorption and photocatalytic experiments*

The photocatalyst layer was performed following the procedure described in [23, 24] and is summarized in the Supplementary Information: Deposition of the $TiO_2$-rGO layer on the ATR crystal. Prior to starting, an infrared spectrum of the P25-rGO film was taken as a background. Two groups of blank reference spectra in the dark and under irradiation were obtained by adding 3 mL of Milli-Q water to the cell. Then, the sample was allowed to equilibrate with the water for 45 min in the dark and infrared spectra were recorded every 300 s. When the last spectrum was collected, the film was irradiated with UV-A light and a new set of spectra were collected every 300 s for 2 hours. Right after both groups of blank spectra were recorded, the water was replaced by 3 mL of a 1 mM oxalic acid (OA) solution at pH 5 adjusted by adding KOH. Two new groups of spectra were monitored in the dark and under UV-A light irradiation. The final spectra were obtained by subtracting the corresponding blank. FTIR spectra were collected at room temperature using a FTIR spectrometer (IFS 66 BRUKER) equipped with an internal reflection element 45º ZnSe crystal and a deuterated triglycine sulphate (DTGS) detector. The interferometer and the infrared light path in the spectrometer were constantly purged with Argon to avoid $H_2O$ and $CO_2$ contamination. Spectra were recorded in the 1800-1200 $cm^{-1}$ region, employing a resolution of 4 $cm^{-1}$ and an averaging of 300 scans.

The samples were irradiated with UV-A light using a LED lamp (Model LED-Driver, THORLABS) emitting 365 nm UV light (FWHM = 7.5 nm). The lamp was placed at a distance of ca. 30 cm from the surface of the test solution to achieve an intensity of UV-A light of 1.0 $mW \cdot cm^{-2}$, measured by an UV radiometer (Dr. Hönle GmbH, Martinsried, Germany).

*2.6 Photocatalytic activity*

The photocatalytic degradation measurements were carried out using a 0.25 L semi-continuous cylindrical reactor made of borosilicate glass and placed under four fluorescent lamps (PHILIPS CLEO 15 W, 365 nm, FWHM = 20 nm) used as an irradiation source. The distance to the lamps from the reactor was adjusted so that the average UV-A flux value was 1.08 $mW \cdot cm^{-2}$ measured by an UV-A radiometer (LT Lutron UVA Light Meter). The photoreactor was filled with 200 mL of a suspension with 0.20 $g \cdot L^{-1}$ of the hybrid photocatalysts and 1 mM of oxalic acid at pH 5 adjusted by adding KOH. The photocatalytic reactions were performed at room temperature (25-30ºC) and atmospheric pressure. The mixture was continually agitated while bubbling air using an air pump (Elite 801, 1000 $cm^3 \cdot min^{-1}$). Prior to reaction, the mixture was premixed for 4 hours in darkness to allow adsorption equilibrium to be reached. Samples were taken out every 15 minutes to follow the reaction and filtered using 0.2 µm-pore-size PTFE syringe filters.

High Performance Ionic Chromatography, HPIC, was used to identify and quantify oxalic acid concentration in a DIONEX ICS-1000 with a conductivity detector and an electro-regenerator-suppressor. An Ion Pac AS9-HC 2 x 250 mm and a guard column Ion Pac AG9-HC 2 x 50 mm from DIONEX was used. The eluent was an alkaline solution of $8 \cdot 10^{-3}$ $mol \cdot L^{-1}$ $Na_2CO_3$ and $1.5 \cdot 10^{-3}$ $mol \cdot L^{-1}$ $NaHCO_3$. The temperature of the detector conductivity cell was kept constant at 35 ºC.

*2.7 EPR study*

Generation of hydroxyl radical and superoxide radical anions upon UV light irradiation of the synthesized P25-rGO photocatalysts was examined by measuring the EPR signal of the DMPO–$HO^{\bullet}$ and DMPO–$O_2^{\bullet-}$ species, respectively. EPR spectra were recorded at room temperature on a MiniScope X-band EPR spectrometer (MS400 Magnettech GmbH, Germany) operating at 9.43 GHz field modulation. The acquisition parameters to detect DMPO–$HO^{\bullet}$/ DMPO–$O_2^{\bullet-}$ were as follows: center field: 339mT, sweep width: 8/6 mT, sweep time: 25/15 s, number of scan: 1, modulation amplitude: 0.1 mT, power: 10 mW, gain: 5. The experimental EPR spectra acquisition and simulation were carried out using MiniScope and Winsim 2002 software. For the sample preparation, the photocatalyst ($1 g \cdot L^{-1}$) was suspended in water or DMSO to detect DMPO–$HO^{\bullet}$ or DMPO–$O_2^{\bullet-}$, respectively, and the suspension were subsequently dispersed by using an ultrasonic bath. Prior to the measurement, 1 mL of the suspension was introduced into the Eppendorf tube and then 200 µL of 40 mM of DMPO were immediately added. The tube was shaken by hand to

homogenize the sample. The suspensions were transferred immediately to 50 µL borosilicate capillaries (Hirschmann ringcaps). The samples were irradiated directly in the EPR spectrometer microwave cavity by a spot UV-light (LC8, Hamamatsu, 200W super-quiet mercury-xenon lamp) through the quartz window of the cell.

## 3. RESULTS AND DISCUSSION

### *3.1 Characterization of P25-rGO composites*

In order to confirm the $TiO_2$ modification with rGO and to characterize the crystal structure of the carbon materials Raman spectroscopy was applied. Figure 1 shows the Raman spectra of GO and of P25-rGO nanohybrid materials with different rGO mass doping ratio. All the $TiO_2$ based samples exhibited four different peaks corresponding to the vibration modes of anatase located at 145 $cm^{-1}$ ($E_g$), 396 $cm^{-1}$ ($B_{1g}$), 517 $cm^{-1}$ ($B_{1g}$+ $A_{1g}$), and 638 $cm^{-1}$ ($E_g$) [6, 25]. As for GO, two different peaks ascribed to the D band and to the G band were observed at 1340 and 1605 $cm^{-1}$, respectively. These two bands were also present in the Raman spectrum of the composites, proving the presence of rGO. Whereas the D peak is attributed to internal structural defects, edge defects or dangling defects caused by the existence of different oxygen-containing functional groups in the case of GO, the G peak is ascribed to C-C and C=C bonds [2, 26]. Hence, a narrow G peak indicates a low amount of functional groups. The area under both peaks was calculated and the ratio $A_D$/ $A_G$ was compared. While GO yielded an $A_D$/ $A_G$ value close to 1.13, indicating a disordered structure [6, 27], values of 1.44, 1.44 and 1.37 were estimated for P25-rGO 0.1%, P25-rGO 0.5%, and P25-rGO 1%, respectively. The ratio between the areas of both peaks increases as a consequence of the strong interaction between $TiO_2$ and rGO sheets, giving rise to a higher disorder degree and suggesting the reduction of GO and the contribution of remaining oxygenated functional groups [6, 7, 25, 28].

To further study the interaction between $TiO_2$ and rGO and their effect on the light absorption, diffuse reflectance UV-vis spectroscopy measurements were conducted. Figures 2A and 2B show the diffuse reflectance spectra of the different P25-rGO films and the Tauc plots, respectively. When the absorption spectra of the samples are evaluated, it could be noted that the higher the rGO content, the higher the absorption in the visible light range. The optical band gap energy of the samples was determined through the Tauc plots. Optical band gap values of 3.1 eV were found for pure $TiO_2$, P25-rGO 0.1%, P25-rGO 0.5% and P25-rGO 1%, respectively, which indicates that the band gap energy remained unchanged by the introduction of rGO. So, as a result the variation is negligible and modification of $TiO_2$ with rGO does not show a reduction of the band gap energy [15, 25].

The XRD patterns of pure GO and P25-rGO composites are shown in Figure S.1. Although of GO exhibited a strong diffraction peak at 11º, this peak was not observed for any of the P25-rGO nanocomposites, which consisted of the characteristic peaks of anatase and rutile

crystalline phases. This could be explained because of the reduction of GO to rGO and the relatively low amount and intensity of rGO/GO compared to the peaks of $TiO_2$ [7, 14, 29].

To analyze the morphology and structure of the photocatalysts SEM and TEM were used. Some images of P25-rGO 0%, P25-rGO 0.5 % and P25-rGO 1% can be seen in Figure 3. From Fig. 3A and Fig.3B it can be noted that primary particles have uniform shape and size for both samples. These primary particles were observed to be densely agglomerated. In Figure 3B an rGO sheet loaded with $TiO_2$ particles could be detected. A detailed insight into the microstructure of the P25-rGO 1% agglomerates is shown in the TEM micrograph of Figure 3C. The picture exhibits $TiO_2$ particles with a size ranging between 15 and 40 nm. The presence of graphene oxide is also evident in some areas. Through HRTEM we have located regions where the $TiO_2$ particles appear surrounded by some sheets of graphene oxide as can be seen in Figure 3D. The picture displays at least two or three particles surrounded by a wrinkled graphene sheet (Marked with red arrows). Fig. 3E displays one of these particles at higher magnifications. As can be deduced from its FFT (Fast Fourier Transform, figure 3F) the particle is oriented along the [111] zone axis of the anatase phase. Although the partially reduced graphene oxide is recovering part of the particles, it also seems to interconnect them proving an intimate contact between $TiO_2$ and rGO that should improve electron transfer from the photo-excited $TiO_2$ to rGO.

One of the most significant properties of semiconductors is the absolute position of the conduction and valence band edges as the possibility of an electron transfer to take place depends on the band potentials. In order to know whether the coexistence of $TiO_2$ and rGO may shift the band position, electrochemical impedance spectroscopy experiments were carried out at different potentials. Values of the space charge layer capacitance ($C_{SC}$) were derived by fitting the impedance spectra at each potential to a Randles circuit. The value of exponential parameter of the CPE was found to be between 0.9 and 1.0. Afterwards, Mott-Schottky plots were constructed by depicting the inverse square of the $C_{SC}$ per unit of area against the respective applied potential (Figure 4). Mott-Schottky plots showed a linear regimen which could be extrapolated to the x axis to obtain the flat-band potential ($E_{FB}$) [8, 16]. By the slope of the plots it was determined that the studied photocatalysts are n-type semiconductors [16]. The flat-band potentials of P25-rGO 0%, P25-rGO 0.5% and P25-rGO 1% were -0.28, -0.27, and -0.29 V vs. RHE respectively. Therefore, as expected, no shift of the $E_{FB}$ was observed when $TiO_2$ was modified with rGO. It is generally known that the conduction band edge ($E_{CB}$) of an n-type semiconductor is around 0-0.2 V more negative than the $E_{FB}$ [30-32]. In this study a value of 0.1 V was chosen and the estimated conduction band potentials for P25-rGO 0%, P25-rGO 0.5%, and P25-rGO 1% were -0.38, -0.37, and -0.39 V vs. RHE, respectively. Taking into account the value of the band gap energies obtained from optical spectroscopy, the values of the valence band potentials were also

estimated (2.76 V, 2.75 V, and 2.75 V vs. RHE for P25-rGO 0%, P25-rGO 0.5%, and P25-rGO 1%, respectively).

To understand the difference in the electronic properties of pure $TiO_2$ and rGO modified titania, the photocurrent response was measured as it provides useful information about the generation and separation of the photogenerated electron-hole pairs under irradiation [7, 33]. Figure 5 illustrates the photocurrent response of the films at 0.8 V bias potential vs. RHE in a 0.1 M $Na_2SO_4$ aqueous solution containing 10% v/v $CH_3OH$ under chopped UV-vis irradiation (A) and visible irradiation (λ > 450nm) (B). In both figures, it can be noted that the photocurrent responses promptly decrease when the light is switch off and comes back to the maximum value when the light is turned on again, showing a good reproducibility of the different cycles. When the samples were irradiated with UV-vis irradiation (Figure 5A) the photocurrent values obtained for P25-rGO 1% and P25-rGO 0.5% were around 6.5 and 3.75 $\mu A \cdot cm^{-2}$ respectively, being 10 and 6 times higher than those values obtained for P25-rGO 0%. This effect in the photocurrent cycles could be attributed to the rGO /$TiO_2$ coupling which allows a faster transfer of the photogenerated electrons from the conduction band of $TiO_2$ to rGO and further transfer to the electrode. When the films were irradiated with visible light (Figure 5B) the photocurrent response followed the same sequence. However, photocurrent values less than 1% were reached when irradiating with wavelength higher than 450 nm. In both figures, a slow photocurrent response of P25-rGO 0% could be ascribed to the electrons trapped in trapping sites such as $Ti^{3+}$. The photogenerated electrons are first trapped in surface or shallow bulk trap sites and further migrate to deeper states, becoming less mobile [5, 34]. Therefore, while the “trap filling” process is taking place, only part of the photogenerated electrons can be transferred to the FTO leading to the slow increase of the photocurrent response [35]. The slow photocurrent fall when the light was turned off could be the result of stored electrons in rGO being released gradually [7]. To sum up, the photocurrents results reveal that more effective charge separations of the photogenerated electron-hole pairs were attained with rGO modified $TiO_2$. This is mainly due to the higher conductance values when rGO was present, which enables a faster charge carrier transfer between the film and the electrode [26, 33].

Electrochemical impedance spectroscopy (EIS) was carried out to obtain the respective Nyquist plots (Figure 6). From these graphs, information about the electron-transfer process across the semiconductor-electrolyte interface can be obtained. It can be noted that the greater the amount of rGO mass concentration, the smaller the semicircle radius, which indicates a more efficient charge separation and lower interfacial charge transfer resistance [7, 25, 36]. A more detailed explanation related to this conclusion is included in the Supplementary Information: Nyquist plot explanation.

In most photocatalytic applications the only electron acceptor available is oxygen. Therefore, the reduction process of oxygen by the photogenerated electrons is crucial. The formation of superoxide anion radicals ($O_2^{\bullet-}$) and hydrogen peroxide ($H_2O_2$) by oxygen reduction by one or more electrons is especially important when the photocatalysts are irradiated by visible light, as previously reported in water disinfection [10, 37]. The different oxygen reduction reactions depending on the number of electrons involved and their respective reduction potentials are shown below [8, 38]:

$$O_2 + H^+ + e^- \rightarrow HO_2^{\bullet} \qquad E_0 = -0.05\, V_{RHE} \qquad (1)$$

$$O_2 + 2H^+ + 2e^- \rightarrow H_2O_2 \qquad E_0 = 0.70\, V_{RHE} \qquad (2)$$

$$O_2 + 4H^+ + 4e^- \rightarrow 2H_2O \qquad E_0 = 1.23\, V_{RHE} \qquad (3)$$

Linear sweep voltammetry experiments were performed to measure the oxygen reduction currents and thus analyze the effect of rGO coupling with $TiO_2$ on the reduction mechanism of oxygen (Figure 7).

The unmodified $TiO_2$ exhibited a negligible oxygen reduction current at potentials above 0 V vs. RHE (< 3 $\mu A \cdot cm^{-2}$), pointing out that a slow reduction process occurred. On the other hand, when titanium dioxide was modified by rGO, a significant rise of the oxygen reduction current was detected up to 0.4 V vs. RHE. The reduction current values obtained at 0 V vs. RHE for P25-rGO 1% (> 23 $\mu A \cdot cm^{-2}$) and P25-rGO 0.5% (< 12 $\mu A \cdot cm^{-2}$) were nearly 10 and 5 times higher than the value reached by P25-rGO 0% (2.4 $\mu A \cdot cm^{-2}$). In conclusion, the higher the amount of rGO in the nanocomposite, the larger the increase of the reduction current, probably because of the lower charge transfer resistance of these photocatalysts.

*3.2 Photocatalytic activity of P25-rGO composites*

To investigate the photocatalytic activity of P25-rGO 0% and P25 modified with rGO, the degradation of 1 mM oxalic acid aqueous solution under UV-A irradiation was followed using ATR-FTIR. In situ ATR-FTIR is a useful technique to characterize the adsorbed species on the photocatalyst surface and monitoring the photodegradation of the surface complexes and intermediates adsorbed [23, 39-41]. Oxalic acid was chosen since it is a model compound which is usually generated as an intermediate during the degradation of more complex pollutants, e.g. phenolic compounds, and because of its simple oxidation pathway [23, 39]. Oxalic acid is transformed into $CO_2$ and the process can be monitored in an easy way since few intermediates (formic acid or carbonates) are formed [39, 41].

Firstly, measurements were carried out to follow the adsorption process for 45 minutes. Figure S.2 shows the time evolution of the recorded spectra of adsorbed oxalic acid in the dark (the time interval between every spectra was 5 min). Several studies have previously shown the main features of FTIR spectrum of oxalic acid adsorbed on $TiO_2$ [39, 40]. In brief,

the band between 1800 and 1600 $cm^{-1}$ and the shoulder at 1590 $cm^{-1}$ were assigned to C=O symmetric stretching mode and O–C=O asymmetric stretching mode. In the region between 1500 and 1200 $cm^{-1}$ two bands could easily be differentiated at around 1420 and 1300 $cm^{-1}$. The first band could be ascribed to the symmetric stretching mode of C-O, C-C, and O-C=O bonds, whereas the second peak rise as a consequence of symmetric stretching mode of C-O bonds overlapping with the bending mode of the O-C=O bonds. A shoulder close to the peak observed at 1300 $cm^{-1}$ has also been related to outer sphere complexes in the case of rutile [40]. By looking at the time evolution of the recorded spectra it could be noticed that the oxalic acid has been mostly adsorbed during the first five minutes, regardless of the nanocomposite. Afterwards, only a slight increase of the intensity was detected, especially, the intensity of the shoulder between 1620 and 1580 $cm^{-1}$ changes slightly, and the equilibrium appeared to be reached after 25 minutes. The evolution of the integrated area of the peaks between 1800 and 1200 $cm^{-1}$ as a function of time is depicted in Figure 8. Only slight changes of the integrated area corresponding to adsorbed oxalic acid was detected after the high value was obtained at 5 minutes. All the curves from the integrated spectra revealed a behavior similar to a Langmuir adsorption isotherm [40], despite the fact that the titanium dioxide was modified with rGO. Comparing the values of the integrated area reached by the studied photocatalysts a rise of the amount of adsorbed oxalic acid was detected when the rGO concentration in the $TiO_2$ increased. This result may be attributed to the high surface area and high selectivity exhibited by rGO [42, 43].

Subsequent to the adsorption process of oxalic acid on the photocatalyst surface, a series of spectra were recorded to track the oxalic acid degradation when the sample was irradiated by 365 nm light with an intensity of 1.0 $mW \cdot cm^{-2}$ for 2 hours. The time evolution of the recorded spectra of the adsorbed organic compound during illumination with UV-A light is displayed in Figure S.3. Following the first spectrum a decrease of the intensity in the wavenumber region between 1620 and 1550 $cm^{-1}$ was observed. This is related to removal of the least stable surface complex that represents the adsorption of oxalate [23, 40]. On the other hand, the peak at 1300 $cm^{-1}$ barely suffered any changes under irradiation.

To better compare these results, the area under the peaks in the region between 1800 and 1200 $cm^{-1}$ was estimated for the spectra recorded every 5 minutes (Figure 9). A pseudo-first order kinetic was observed for the oxalate surface photodegradation reaction. The obtained pseudo-first order rate constants were $5.2 \cdot 10^{-3 \pm} 2.3 \cdot 10^{-4}$, $5.5 \cdot 10^{-3 \pm} 2.1 \cdot 10^{-4}$, $5.7 \cdot 10^{-3 \pm} 1.2 \cdot 10^{-4}$ and $6.8 \cdot 10^{-3 \pm} 1.7 \cdot 10^{-4}$ $min^{-1}$ for P25-rGO 0%, P25-rGO 0.1%, P25-rGO 0.5%, and P25-rGO 1%, respectively. The modified $TiO_2$ with 0.5% and 1% yielded slightly higher values of the pseudo-first order kinetic constant than pure $TiO_2$ (1.1 and 1.3 times higher respectively). This slight rise could be attributed to the higher adsorption capacity as a result of the

introduction of rGO, previously mentioned above, and the more efficient separation of the photogenerated charge carriers according to the electrochemical characterization.

To further investigate the photocatalytic degradation of oxalic acid, reactions in which the photocatalysts were suspended in a 1 mM oxalic acid aqueous solution were conducted. UV-A light with an intensity of 1.08 $mW \cdot cm^{-2}$ was used to irradiate the reactor. No photolysis of oxalic acid was previously reported [44, 45]. The photocatalytic degradation of oxalic acid over different studied photocatalysts is shown in Figure 10 as the plot of the oxalic acid concentration versus illumination time. In this case, even smaller differences were observed in the photocatalytic degradation curves obtained for the nanocomposites compared to the studies using ATR-FTIR spectroscopy. One of the advantages of characterizing the photocatalytic oxidation using the ATR-FTIR technique is that differences of the effective path lengths are diminished as a thin layer is deposited on the ATR crystal. However, when the photocatalyst is suspended in the reaction medium, light-block effects occur. For instance, an excess of rGO can block the amount of light reaching the $TiO_2$ nanoparticles [25], leading to lower photonic efficiencies in spite of the other beneficial properties of rGO. That might be the reason why P25-rGO 0.5% yielded the highest photodegradation in suspension, even though the surface photocatalytic reaction was faster for P25-rGO 1% as was shown by the ATR-FTIR experiments. Furthermore, an excessive amount of rGO could lead to the formation of clusters or agglomerates acting as recombination centers [25, 46].

Despite the fact that the electrochemical characterization indicated that the modification of $TiO_2$ with rGO led to much more efficient separation of the photogenerated charge carriers, similar photodegradation kinetics were observed for the different photocatalysts used in this study. In order to evaluate the effect of the mass doping ratio of rGO on the role played by the photogenerated electrons and holes and their influence in the photocatalytic mechanism under UV light, EPR measurements were performed to detect the reactive oxygen species (ROS) involved in the photocatalytic process. Dissolved molecular oxygen plays a crucial role since it reacts with trapped electrons, subsequent to being photogenerated, forming superoxide anion radicals ($O_2^{\bullet-}$) [37]. The generation of $O_2^{\bullet-}$ was detected at room temperature by performing spin trapping technique using DMPO. The photocatalysts were suspended in DMSO instead of water to avoid the facile disproportionation of the superoxide radical that leads to a slow reaction between superoxide anion radicals or hydroperoxyl radicals and DMPO [47]. Moreover, using DMSO as a solvent favors the generation and trapping of $O_2^{\bullet-}$ because of the stabilization effect of the aprotic solvent and the higher solubility of molecular oxygen [48]. Figure S.4 displays EPR spectra obtained at different irradiation times of the P25-rGO suspensions saturated with $O_2$. Under these conditions, for all the studied photocatalysts, a series of peaks were observed immediately after irradiation at around 337 mT and 340,5 mT for example. Then they decayed at the same time the

intensity of other peaks at 336,5 mT and 338 mT increased. The simulation analysis of the EPR spectra (Figure S.5) revealed that the interaction of EPR signals could be ascribed to a combination of DMPO–$O_2^{\bullet-}$ ($a_N$ = 1.282 mT, $a_H^{\beta}$=1.035 mT, $a_H^{\gamma}$=0.132 mT; g = 2.0058) and $^{\bullet}$DMPO–$CH_3$ ($a_N$ = 1.462 mT, $a_H^{\beta}$=2.093 mT; g = 2.0057) [48, 49], where the two first signals mentioned above were attributed to the DMPO–$O_2^{\bullet-}$ whereas the peaks at 336,5 mT and 338 mT corresponded to the generation of $^{\bullet}$DMPO–$CH_3$. The formation of $CH_3^{\bullet}$ was previously reported as the result of the oxidation of DMSO by $HO^{\bullet}$ radicals generated by the presence of adsorbed water onto the catalyst surface [48, 50].

To delay the generation of $^{\bullet}$DMPO–$CH_3$ and achieve a better comparison of the ability to generate $O_2^{\bullet-}$ radicals, the samples were irradiated for just two seconds, and afterwards, the EPR spectra was recorded (Figure S.6). The simulation confirmed the generation of DMPO–$O_2^{\bullet-}$, characterized by hyperfine splitting $a_N$ = 1.282 mT, $a_H^{\beta}$=1.035 mT, $a_H^{\gamma}$=0.132 mT; g = 2.0058 [48, 49]. Although the differences between these spectra are small, P25-rGO 0.1 and 0.5% exhibit a higher intensity. These results were attributed to the ability to reduce oxygen more easily when the $TiO_2$ was modified by rGO, Figure 7.

Valence band holes react with adsorbed hydroxide anions and water molecules giving rise to hydroxyl radicals, which together with holes are crucial oxidative species in the photocatalytic oxidation of dissolved organic matter [48]. Furthermore, hydroxyl radicals can be formed by consecutive reactions of photogenerated $O_2^{\bullet-}$ with protons from the aqueous solution (reactions 4-7):

$$O_2^{\bullet-} + H^+ \rightarrow HO_2^{\bullet} \quad (4)$$

$$2HO_2^{\bullet} \rightarrow H_2O_2 + O_2 \quad (5)$$

$$H_2O_2 + O_2^{\bullet-} \rightarrow HO^{\bullet} + O_2 + HO^- \quad (6)$$

$$H_2O_2 + e_{Cb}^- \rightarrow HO^{\bullet} + HO^- \quad (7)$$

The detection of hydroxyl radicals was performed upon irradiation of P25-rGO in $O_2$ and $N_2$ saturated aqueous suspensions at room temperature (Figure S.7). No signal was measured in the dark for any of the photocatalysts. However, when the sample was irradiated by a Xe lamp, a four-line EPR signal was identified. The simulation analysis, Figure S.8, confirmed the generation of DMPO–$HO^{\bullet}$ ($a_N$ = 1.497 mT, $a_H$ = 1.477 mT; g = 2.0057) [48, 49].

It can be noticed that the experimental spectra perfectly corresponded with the simulated one. The signal appeared immediately after exciting the sample and suffered a decreased in intensity after 30 seconds (Figure S.7). No significant differences were observed among the spectra obtained for the studied photocatalysts, which indicates that a similar concentration of hydroxyl radicals were photogenerated in the presence of rGO. In order to discuss more easily the generation of reactive oxygen species in EPR experiments, the area of the EPR spectra signals, obtained under the different atmospheres, were calculated and plotted

versus rGO mass concentration (Figure 11). Similar values for DMPO–$HO^{\bullet}$ and DMPO–$O_2^{\bullet-}$ were found regardless of the rGO doping ratio in $O_2$ saturated suspensions, with P25-rGO 0.5 % yielding the highest integrated area for both measured reactive oxygen species, $O_2^{\bullet-}$ and $HO^{\bullet}$. The slight increase detected for some of these nanocomposites could be ascribed to the most effective separation of photogenerated charge carriers and the ability to achieve a more efficient reduction of oxygen. Regarding P25-rGO 1%, the integrated area values decreased as a result of the shielding effect caused by an excess of rGO that could also imply the formation of clusters acting as recombination centers [15, 46], as was already pointed out in the above discussion about oxalic acid photodegradation. However, when the DMPO–$HO^{\bullet}$ EPR spectra measured in $N_2$ saturated suspensions was integrated, the integrated area was found to increase three times when 0.1% rGO was incorporated to $TiO_2$. Higher rGO concentrations only led to a slight increase. These results evinced the role played by rGO as an electron acceptor which enables the reaction between holes and adsorbed water to generate hydroxyl radicals whereas the electrons are dragged to rGO.

Even though electrochemical results indicated a great enhancement in separating electron-hole pairs, only a small improvement of photocatalytic activity was found in oxalic acid experiments and in ROS detection. To better understand of the processes occurring upon illumination transient absorption spectroscopy (TAS) has been conducted in the microsecond scale, which allows studying the reaction dynamics of the photogenerated charges. The TAS decays for the $TiO_2$ and $TiO_2$-rGO powders under $N_2$ or $O_2$ were obtained after exciting the sample with laser pulses of light with a wavelength of 355 nm and energy of 2.2 mJ $cm^{-2}$ per pulse (Figure 12). Probe wavelengths at 400 nm and 660 nm were used to follow the decay kinetics of the trapped holes and electrons, respectively [5, 51-55].

A kinetic model based on fractal surfaces [21] was applied to evaluate the effect of rGO and the atmosphere on the charge carriers dynamics:

$$\Delta J = \frac{A(1-h)}{(1-h) + Ak_f t^{1-h}} \quad (8)$$

Where $k_f t^{-h}$ represents a rate coefficient and a time dependent factor, h is related to the fractal dimension of the surface and A represents the height of the transient signal. The $k_f$ and A parameters are shown in Table 1.

Since rGO acts as an electron acceptor, electrons are transferred from $TiO_2$ to rGO in the ps time regime [5, 55]. That's why the A parameters and the initial signals from trapped electrons (660 nm), observed in Table 1 and Figure 12, were less intense compared to bare $TiO_2$ in both atmospheres. It seems that 0.5% is the optimal rGO mass doping ratio because a higher addition of rGO does not mean a further reduction of the initial transient absorption signal. It is noteworthy that in $O_2$ atmosphere the initial intensity obtained by bare $TiO_2$ at 660 nm was lower than that obtained in $N_2$ atmosphere. On the other hand, the initial height of

the P25-rGO photocatalysts rose compared to the intensity observed in $N_2$ atmosphere. The lowest initial intensity at 660 nm in $O_2$ was observed for P25-rGO 0.5% indicating that a more electrons were transferred either to rGO or to $O_2$. All in all, the initial intensity difference between bare $TiO_2$ and P25 modified with rGO, and therefore the electron transfer, was considerable decreased in the presence of $O_2$. These results agreed with the EPR results. Whereas low differences in DMPO–$O_2^{\bullet-}$ and DMPO–$HO^{\bullet}$ areas were noted in the presence of $O_2$, with P25-rGO 0.5% yielding the best results, the DMPO–$HO^{\bullet}$ areas measured for the $TiO_2$-rGO nanocomposites was much higher than that obtained for P25-rGO 0% in $N_2$ atmosphere.

As for the rate coefficients, $k_f$ values estimated from the TAS decays in $N_2$ atmosphere increased with the rGO content becoming between four and ten times higher than those for P25-rGO 0%. In TAS studies carried out in the μs time scale, the recombination between trapped electrons and holes was observed [5]. Thus, results indicates that in $N_2$ atmosphere, where electrons cannot be released, rGO acts as a recombination center that leads to a faster charge carrier recombination rate [55]. On the other hand, in $O_2$ atmosphere $k_f$ values were reduced when rGO was added to $TiO_2$. Hence, the charge carrier recombination rate was decreased, and thus it could lead to higher $O_2^{\bullet-}$ generation rate.

Concerning the 400 nm signal, it could be ascribed to deeply trapped holes that does not affect the photocatalytic activity [55]. This was verified since only small differences in the initial intensity were observed when rGO was added. In the presence of $O_2$, the initial height of the signal increased, due to the presence of an electron scavenger that reduced the recombination rate. Apart from that, the decay constants $k_f$ increased with the addition of rGO and were similar in both atmospheres. However, it was previously corroborated that the charge carrier recombination rate was decreased in the presence of $O_2$. Hence, the decay rates observed at 400 nm was attributed to the migration of holes between different trapping sites (after electrons were transferred from $TiO_2$ to rGO) [55].

To sum up, the presence of $O_2$ hinders the transfer of free electrons from $TiO_2$ to rGO but favors the electron transfer from bare $TiO_2$. In other words, the role of rGO as an electron acceptor is less significant in $O_2$ atmosphere. As a consequence, lower differences in the $O_2^{\bullet-}$ and $HO^{\bullet}$ generation between bare $TiO_2$ and P25-rGO photocatalysts were detected.

## 4. CONCLUSIONS

$TiO_2$-rGO photocatalysts were successively prepared by a hydrothermal method. The junction between $TiO_2$ and rGO involved a higher disorder degree as a consequence of the strong interaction between $TiO_2$ and rGO sheets. However, it did not mean a change of the surface area or the XRD patterns. Besides, the optical band gap and the conduction and valence band potentials were unchanged by the modification of $TiO_2$ with rGO, measuring

values around -0.38 and 2.75 V vs. RHE, respectively. Electrochemical impedance spectroscopy (EIS) and photocurrent response measurements were carried out to evaluate the efficiency of charge separation. The addition of rGO led to a low charge transfer resistance across the electrode-electrolyte interface and even a tenfold increase in the photocurrent values was observed for P25-rGO 1%, indicating a more efficiency in the electron-hole separation.

A higher oxygen reduction current was found when increasing the rGO concentration. This could lead to an enhancement of the generation of reactive oxygen species (ROS). However, in the oxalic acid degradation only small differences were observed. Concerning the surface reaction measured using the ATR-FTIR technique, the higher the amount of rGO added, the higher the adsorption. As a consequence the surface reaction was faster for P25-rGO 1% thanks to a more efficient reduction of oxygen and lower charge transfer resistance, which suggests that this hybrid nanocomposite was also less limited by possible $O_2$ mass transfer limitations. Under slurry photoreactor conditions at oxygen excess, the oxalic acid photo-oxidation evolution was similar for all the studied catalysts. The EPR experiments revealed that only a slight increase of the generated $HO^{\bullet}$ and $O_2^{\bullet-}$ for P25-rGO 0.5% as a result of slightly lower decay kinetics of the photogenerated electrons found in the TAS studies. On the other hand, regarding generation of $HO^{\bullet}$ by $N_2$ saturated suspensions, the addition of only 0.1% rGO mass concentration was enough to detect a threefold increase of the EPR signal related to DMPO–$HO^{\bullet}$. Finally, to relate photocatalytic activity and EPR studies, the role played by rGO was investigated by conducting transient absorption spectroscopy (TAS) experiments under $O_2$ and $N_2$ atmospheres. TAS decay kinetics corroborated that rGO acts as an electron acceptor, occurring the electron transfer from $TiO_2$ to rGO in the ps time scale. This explained the higher DMPO–$HO^{\bullet}$ signal obtained in $N_2$ atmosphere when rGO was added. However, the role played by rGO was not crucial in excess of dissolved $O_2$, which meant lower differences in the $O_2^{\bullet-}$ and $HO^{\bullet}$ generation detected by EPR between bare $TiO_2$ and $TiO_2$ modified with rGO.

**Acknowledgements**

This work has been supported by the Spanish Plan Nacional de I+D+i through the project CTM2015-64895-R and CTM2016-76454-R. Alvaro Tolosana-Moranchel thanks to Ministerio de Educación, Cultura y Deporte for his FPU grant (FPU14/01605).

## 5. REFERENCES

[1] S. Malato, P. Fernández-Ibáñez, M.I. Maldonado, J. Blanco, W. Gernjak, Catalysis Today 147 (2009) 1-59.

[2] P. Fernández-Ibáñez, M.I. Polo-López, S. Malato, S. Wadhwa, J.W.J. Hamilton, P.S.M. Dunlop, R. D'Sa, E. Magee, K. O'Shea, D.D. Dionysiou, J.A. Byrne, Chemical Engineering Journal 261 (2015) 36-44.
[3] J. Carbajo, P. García-Muñoz, A. Tolosana-Moranchel, M. Faraldos, A. Bahamonde, Environmental Science and Pollution Research (2014) 12233-12240.
[4] M. Martín-Sómer, B. Vega, C. Pablos, R. van Grieken, J. Marugán, Applied Catalysis B: Environmental 221 (2018) 258-265.
[5] J. Schneider, M. Matsuoka, M. Takeuchi, J. Zhang, Y. Horiuchi, M. Anpo, D.W. Bahnemann, Chemical Reviews 114 (2014) 9919-9986.
[6] P. Ribao, M.J. Rivero, I. Ortiz, Environmental Science and Pollution Research 24 (2017) 12628-12637.
[7] T. Liu, B. Liu, L. Yang, X. Ma, H. Li, S. Yin, T. Sato, T. Sekino, Y. Wang, Applied Catalysis B: Environmental 204 (2017) 593-601.
[8] J.Z. Bloh, R. Dillert, D.W. Bahnemann, Physical Chemistry Chemical Physics 16 (2014) 5833-5845.
[9] M. Minella, M. Demontis, M. Sarro, F. Sordello, P. Calza, C. Minero, Journal of Materials Science 50 (2015) 2399-2409.
[10] L.L. Tan, S.P. Chai, A.R. Mohamed, ChemSusChem 5 (2012) 1868-1882.
[11] M. Faraldos, A. Bahamonde, Catalysis Today 285 (2017) 13-28.
[12] N. Zhang, M.-Q. Yang, S. Liu, Y. Sun, Y.-J. Xu, Chemical Reviews 115 (2015) 10307-10377.
[13] C. Han, N. Zhang, Y.-J. Xu, Nano Today 11 (2016) 351-372.
[14] K.-Q. Lu, Y. Chen, X. Xin, Y.-J. Xu, Applied Catalysis B: Environmental 224 (2018) 424-432.
[15] M. Minella, F. Sordello, C. Minero, Catalysis Today 281 (2017) 29-37.
[16] H.N.D. Zhebo Chen, Eric Miller, Photoelectrochemical Water Splitting Standards, Experimental Methods, and Protocols, Springer New York, 2013.
[17] M. Cao, P. Wang, Y. Ao, C. Wang, J. Hou, J. Qian, Chemical Engineering Journal 264 (2015) 113-124.
[18] L.L. Tan, W.J. Ong, S.P. Chai, A.R. Mohamed, Chemical Engineering Journal 283 (2016) 1254-1263.
[19] R.L.Z. R. Jenkins, Introduction to X-Ray powder Diffractometry, John Wisley & Sons Inc., New York, 1996.
[20] R.A. Spurr, H. Myers, Analytical Chemistry 29 (1957) 760-762.
[21] F. Sieland, J. Schneider, D.W. Bahnemann, The Journal of Physical Chemistry C (2017).
[22] S. Ito, T.N. Murakami, P. Comte, P. Liska, C. Grätzel, M.K. Nazeeruddin, M. Grätzel, Thin Solid Films 516 (2008) 4613-4619.
[23] C.B. Mendive, D.W. Bahnemann, M.A. Blesa, Catalysis Today 101 (2005) 237-244.
[24] H. Belhadj, S. Melchers, P.K.J. Robertson, D.W. Bahnemann, Journal of Catalysis 344 (2016) 831-840.
[25] A. Morais, C. Longo, J.R. Araujo, M. Barroso, J.R. Durrant, A.F. Nogueira, Physical Chemistry Chemical Physics 18 (2016) 2608-2616.
[26] N.J. Bell, Y.H. Ng, A. Du, H. Coster, S.C. Smith, R. Amal, The Journal of Physical Chemistry C 115 (2011) 6004-6009.
[27] A.W. Morawski, E. Kusiak-Nejman, A. Wanag, J. Kapica-Kozar, R.J. Wróbel, B. Ohtani, M. Aksienionek, L. Lipińska, Catalysis Today 280 (2017) 108-113.
[28] S. Kaniyankandy, S.N. Achary, S. Rawalekar, H.N. Ghosh, The Journal of Physical Chemistry C 115 (2011) 19110-19116.
[29] W. Fan, Q. Lai, Q. Zhang, Y. Wang, The Journal of Physical Chemistry C 115 (2011) 10694-10701.
[30] E. Gao, W. Wang, M. Shang, J. Xu, Physical Chemistry Chemical Physics 13 (2011) 2887-2893.
[31] S. Huang, Q. He, J. Zai, M. Wang, X. Li, B. Li, X. Qian, Chemical Communications 51 (2015) 8950-8953.
[32] H. Yang, J. Tian, T. Li, H. Cui, Catalysis Communications 87 (2016) 82-85.

[33] C. Wang, M. Cao, P. Wang, Y. Ao, J. Hou, J. Qian, Applied Catalysis A: General 473 (2014) 83-89.
[34] Y. Tamaki, A. Furube, M. Murai, K. Hara, R. Katoh, M. Tachiya, Physical Chemistry Chemical Physics 9 (2007) 1453-1460.
[35] J. Yu, G. Dai, B. Huang, The Journal of Physical Chemistry C 113 (2009) 16394-16401.
[36] Q. Wang, N. Zhu, E. Liu, C. Zhang, J.C. Crittenden, Y. Zhang, Y. Cong, Applied Catalysis B: Environmental 205 (2017) 347-356.
[37] B.R. Cruz-Ortiz, J.W.J. Hamilton, C. Pablos, L. Díaz-Jiménez, D.A. Cortés-Hernández, P.K. Sharma, M. Castro-Alférez, P. Fernández-Ibañez, P.S.M. Dunlop, J.A. Byrne, Chemical Engineering Journal 316 (2017) 179-186.
[38] H. Mattila, S. Khorobrykh, V. Havurinne, E. Tyystjärvi, Journal of Photochemistry and Photobiology B: Biology 152, Part B (2015) 176-214.
[39] C.B. Mendive, T. Bredow, M.A. Blesa, D.W. Bahnemann, Physical Chemistry Chemical Physics 8 (2006) 3232-3247.
[40] C.B. Mendive, T. Bredow, A. Feldhoff, M.A. Blesa, D. Bahnemann, Physical Chemistry Chemical Physics 11 (2009) 1794-1808.
[41] C.B. Mendive, T. Bredow, J. Schneider, M. Blesa, D. Bahnemann, Journal of Catalysis 322 (2015) 60-72.
[42] H. Adamu, P. Dubey, J.A. Anderson, Chemical Engineering Journal 284 (2016) 380-388.
[43] H. Zhang, X. Lv, Y. Li, Y. Wang, J. Li, ACS Nano 4 (2009) 380-386.
[44] V. Iliev, D. Tomova, L. Bilyarska, A. Eliyas, L. Petrov, Applied Catalysis B: Environmental 63 (2006) 266-271.
[45] V. Iliev, D. Tomova, S. Rakovsky, A. Eliyas, G.L. Puma, Journal of Molecular Catalysis A: Chemical 327 (2010) 51-57.
[46] J.Z. Bloh, R. Dillert, D.W. Bahnemann, Journal of Physical Chemistry C 116 (2012) 25558-25562.
[47] G. Liu, J. Zhao, H. Hidaka, Journal of Photochemistry and Photobiology A: Chemistry 133 (2000) 83-88.
[48] D. Dvoranová, Z. Barbieriková, V. Brezová, Molecules 19 (2014) 17279.
[49] G.R. Buettner, Free Radical Biology and Medicine 3 (1987) 259-303.
[50] V. Brezová, S. Gabčová, D. Dvoranová, A. Staško, Journal of Photochemistry and Photobiology B: Biology 79 (2005) 121-134.
[51] D.W. Bahnemann, M. Hilgendorff, R. Memming, The Journal of Physical Chemistry B 101 (1997) 4265-4275.
[52] A. Furube, T. Asahi, H. Masuhara, H. Yamashita, M. Anpo, The Journal of Physical Chemistry B 103 (1999) 3120-3127.
[53] Y. Tamaki, A. Furube, R. Katoh, M. Murai, K. Hara, H. Arakawa, M. Tachiya, Comptes Rendus Chimie 9 (2006) 268-274.
[54] T. Yoshihara, R. Katoh, A. Furube, Y. Tamaki, M. Murai, K. Hara, S. Murata, H. Arakawa, M. Tachiya, The Journal of Physical Chemistry B 108 (2004) 3817-3823.
[55] A.O.T. Patrocinio, J. Schneider, M.D. Franca, L.M. Santos, B.P. Caixeta, A.E.H. Machado, D.W. Bahnemann, RSC Advances 5 (2015) 70536-70545.

**Table**

**Table 1. Estimated kinetic parameters of the transient decay signals dependent on the rGO (%) mass concentration and initial transient absorption obtained under $N_2$ and $O_2$ atmospheres.**

| | $N_2$ — $400\ nm$ | | $N_2$ — 660 nm | | $O_2$ — $400\ nm$ | | $O_2$ — 660 nm | |
|---|---|---|---|---|---|---|---|---|
| | $k_f$ (au·μs$^{-1}$)·10$^{-3}$ | A·10$^2$ | $k_f$ (au·μs$^{-1}$)·10$^{-3}$ | A·10$^2$ | $k_f$ (au·μs$^{-1}$)·10$^{-3}$ | A·10$^2$ | $k_f$ (au·μs$^{-1}$)·10$^{-3}$ | A·10$^2$ |
| **P25-rGO 0%** | 2.43 | 2.25 | 5.56 | 1.50 | 2.18 | 2.47 | 4.47 | 0.91 |
| **P25-rGO 0.1%** | 3.41 | 3.12 | 18.53 | 0.85 | 3.91 | 1.65 | 0.58 | 0.73 |
| **P25-rGO 0.5%** | 5.00 | 5.09 | 26.90 | 0.26 | 5.78 | 7.75 | 3.19 | 0.44 |
| **P25-rGO 1%** | 6.91 | 2.78 | 44.32 | 0.60 | 10.17 | 1.15 | 2.95 | 0.51 |

**Figure**

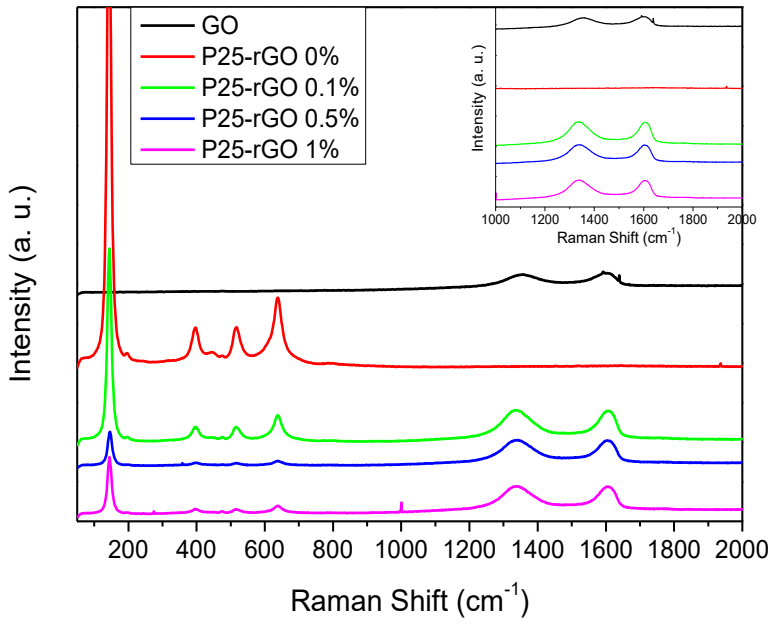


**Figure 1. Raman spectra of GO, P25-rGO 0%, P25-rGO 0.1%, P25-rGO 0.5%, and P25-rGO 1%; and the magnified spectra ranging from 1000 $cm^{-1}$ to 2000 $cm^{-1}$ (upper right).**

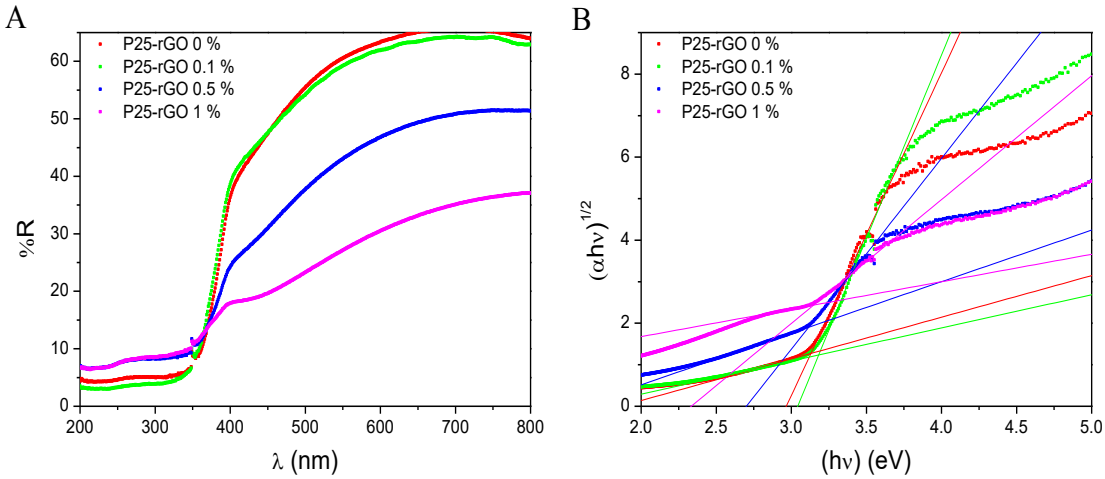


**Figure 2. Diffuse reflectance UV–vis spectra of P25-rGO composites (A) and Tauc plots (B) used to estimate the band gap values. α represents the absorption coefficient.**

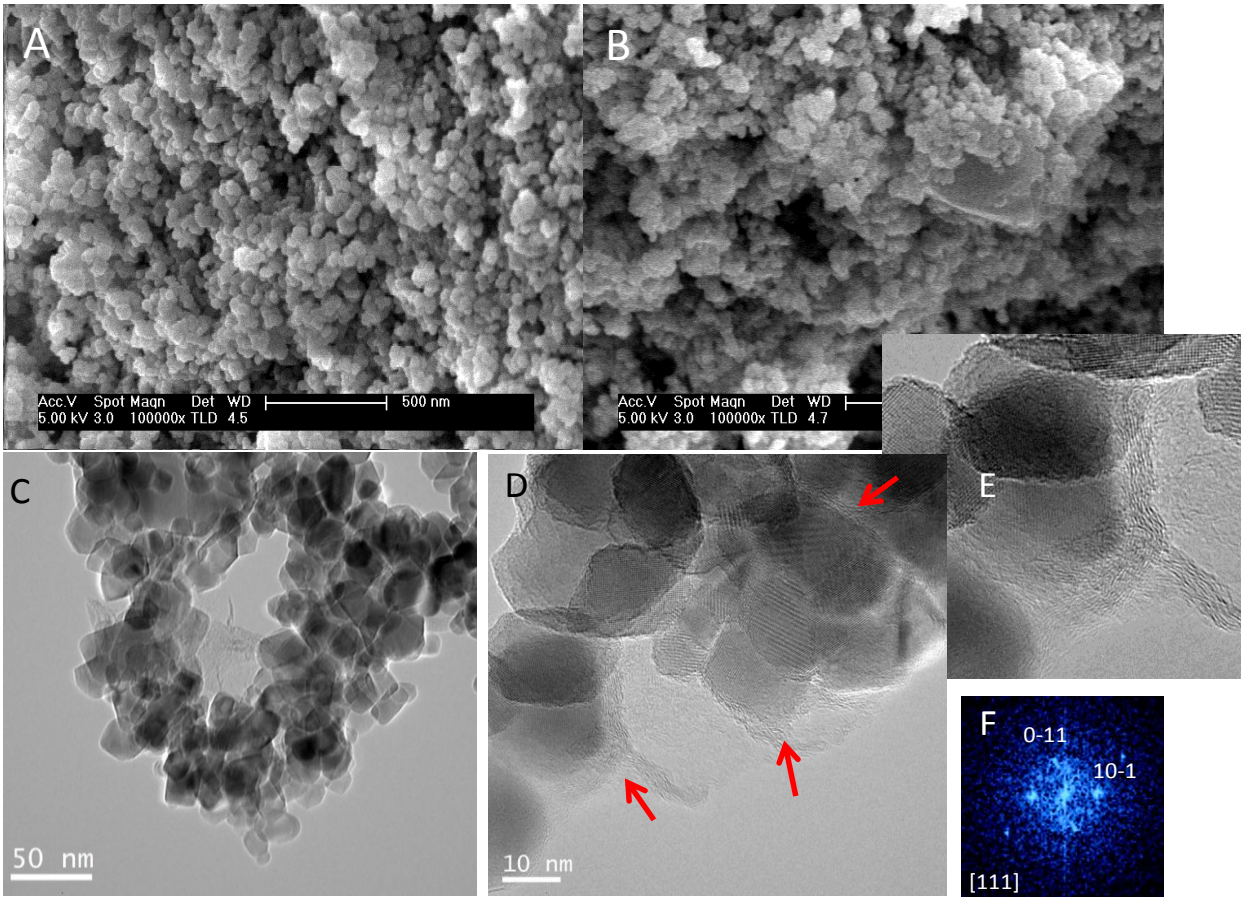


**Figure 3. SEM images of P25-rGO 0% (A) and P25-rGO 0.5% (B). TEM and HRTEM images of P25-rGO 1% (C and D): High magnification of P25-rGO 1% showing the presence of rGO layers (E). Fast Fourier Transform (FFT) of the photocatalyst particles (F).**

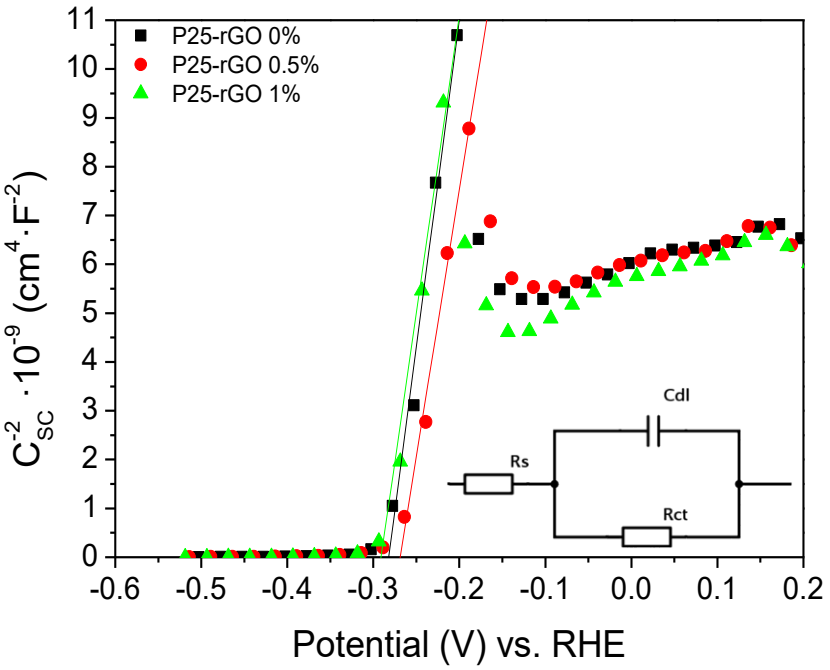


**Figure 4. Mott-Schottky plots of P25-rGO 0%, P25-rGO 0.5% and P25-rGO 1% electrodes. The intercept of the linear regime with the x-axis determines the flat-band potential. The equivalent Randles circuit is inseted.**

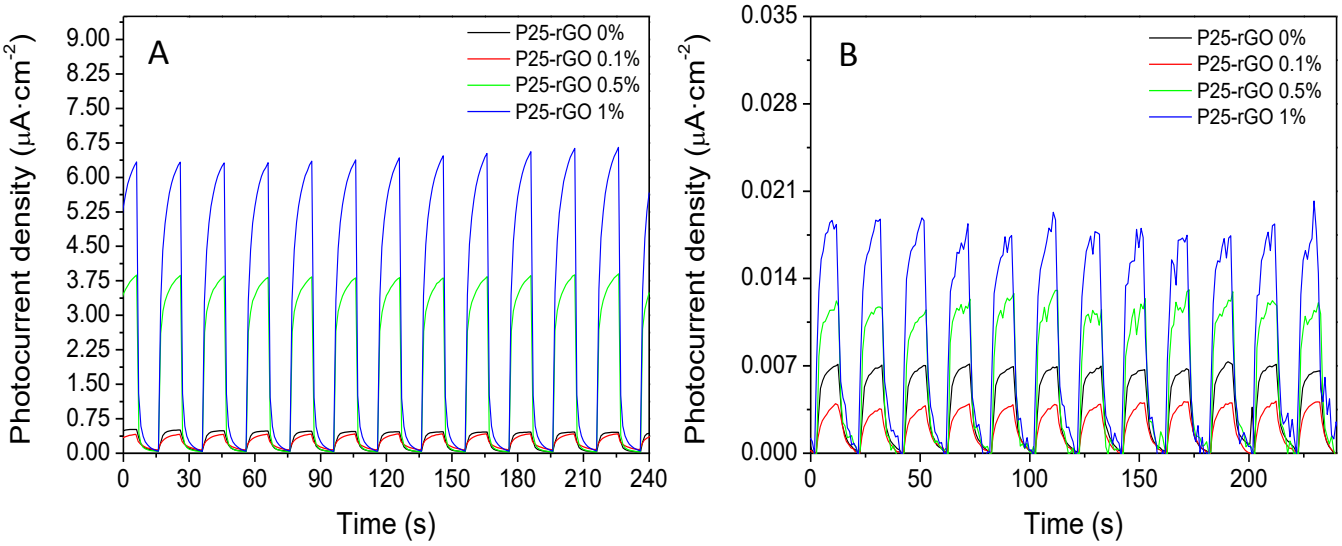


**Figure 5. Photocurrent density versus time curves for the hybrid materials with different rGO mass doping ratio under (A) chopped UV-vis light and (B) chopped visible light (λ > 450 nm).**

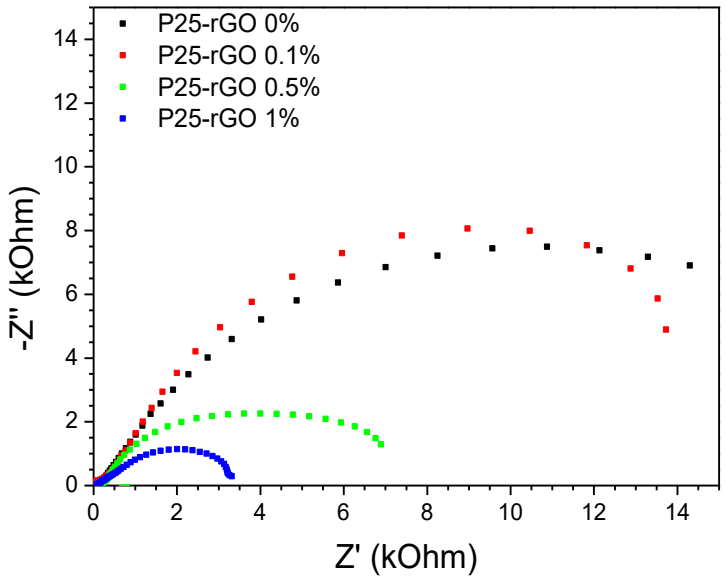


**Figure 6. Nyquist plots measured in 0.1 M $Na_2SO_4$ aqueous solution under 0V bias vs. RHE. The employed frequency range was from 0.1 Hz to 30 kHz.**

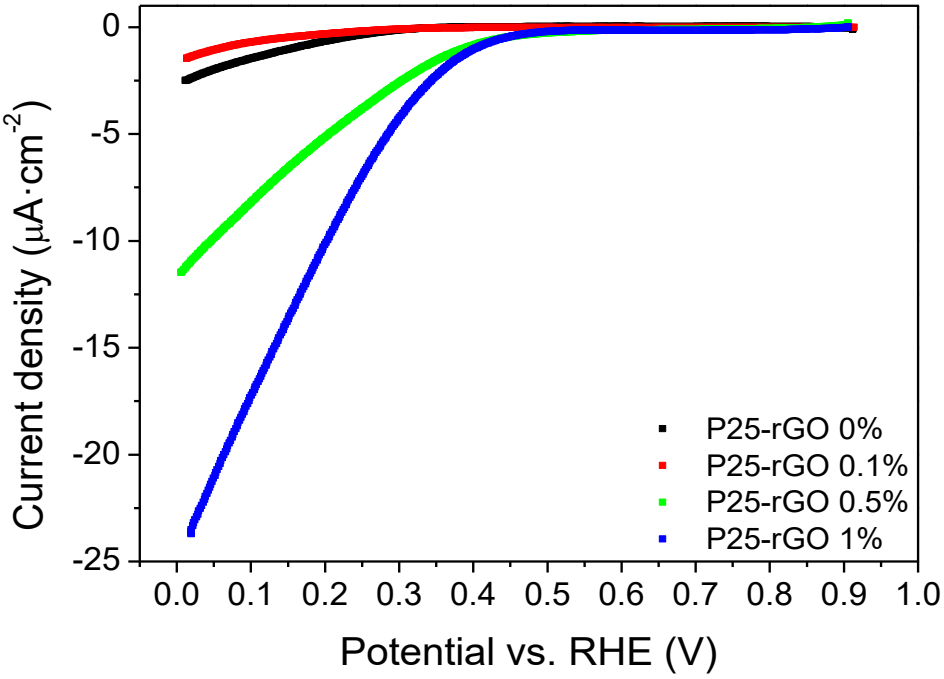


**Figure 7. Oxygen reduction current vs. applied potential for the different modified $TiO_2$.**

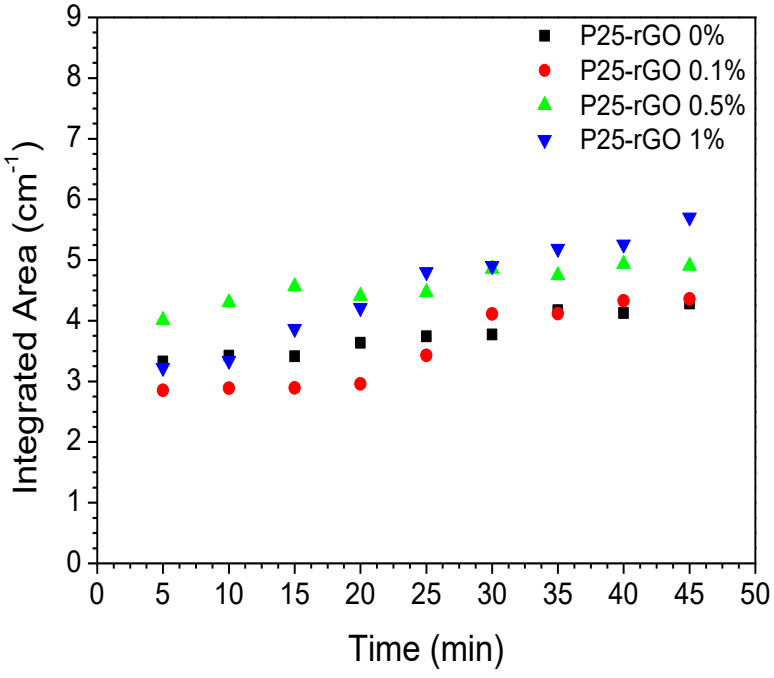


**Figure 8. Time evolution of the integrated IR spectral signals between 1200 and 1800 $cm^{-1}$ of the films in contact with 3 mL of oxalic acid solution in the dark.**

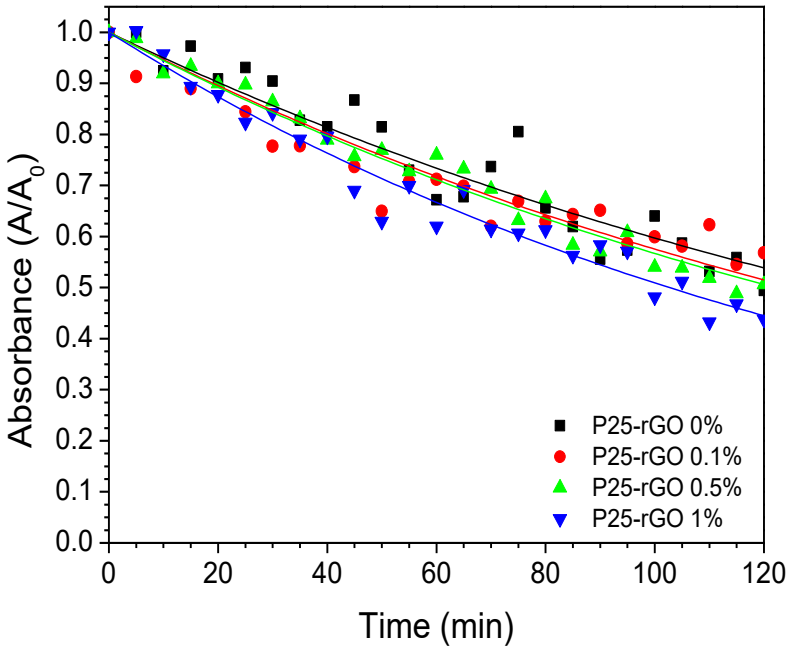


**Figure 9. Time evolution of the integrated area between 1800 and 1200 $cm^{-1}$. A 365 nm LED with an intensity of 1 $mW \cdot cm^{-2}$ was used to illuminate the sample.**

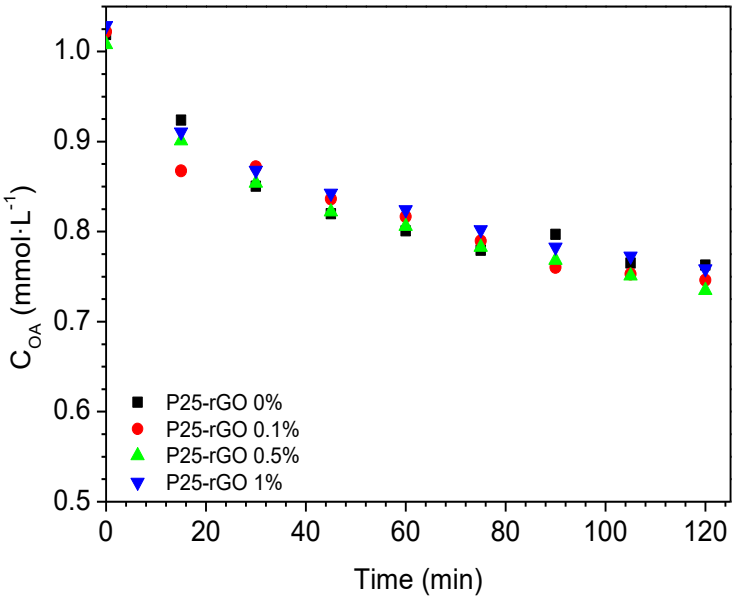


**Figure 10. Time evolution of the concentration of oxalic acid using P25-rGO 0%, P25-rGO 0.1%, P25-rGO 0.5% and P25-rGO 1%. The sample were irradiated with UV-A light with an intensity of 1.08 $mW \cdot cm^{-2}$.**

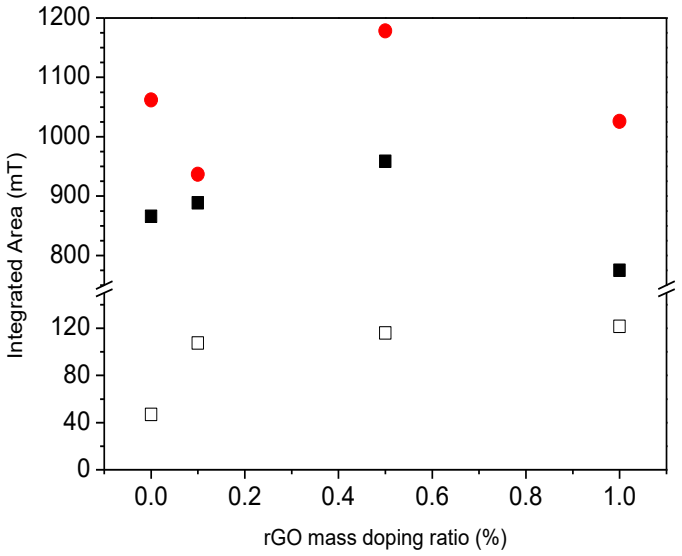


**Figure 11. Calculated area for $^{\bullet}$DMPO–OH adduct in $O_2$ (■), $^{\bullet}$DMPO–$O_2^-$ adduct in $O_2$ (●), $^{\bullet}$DMPO–OH adduct in $N_2$ (□) for the studied P25-rGO photocatalysts. The area of the $^{\bullet}$DMPO–OH and $^{\bullet}$DMPO–$O_2^-$ adducts were calculated from the EPR spectra obtained after illuminating for 30 and 2 seconds respectively.**

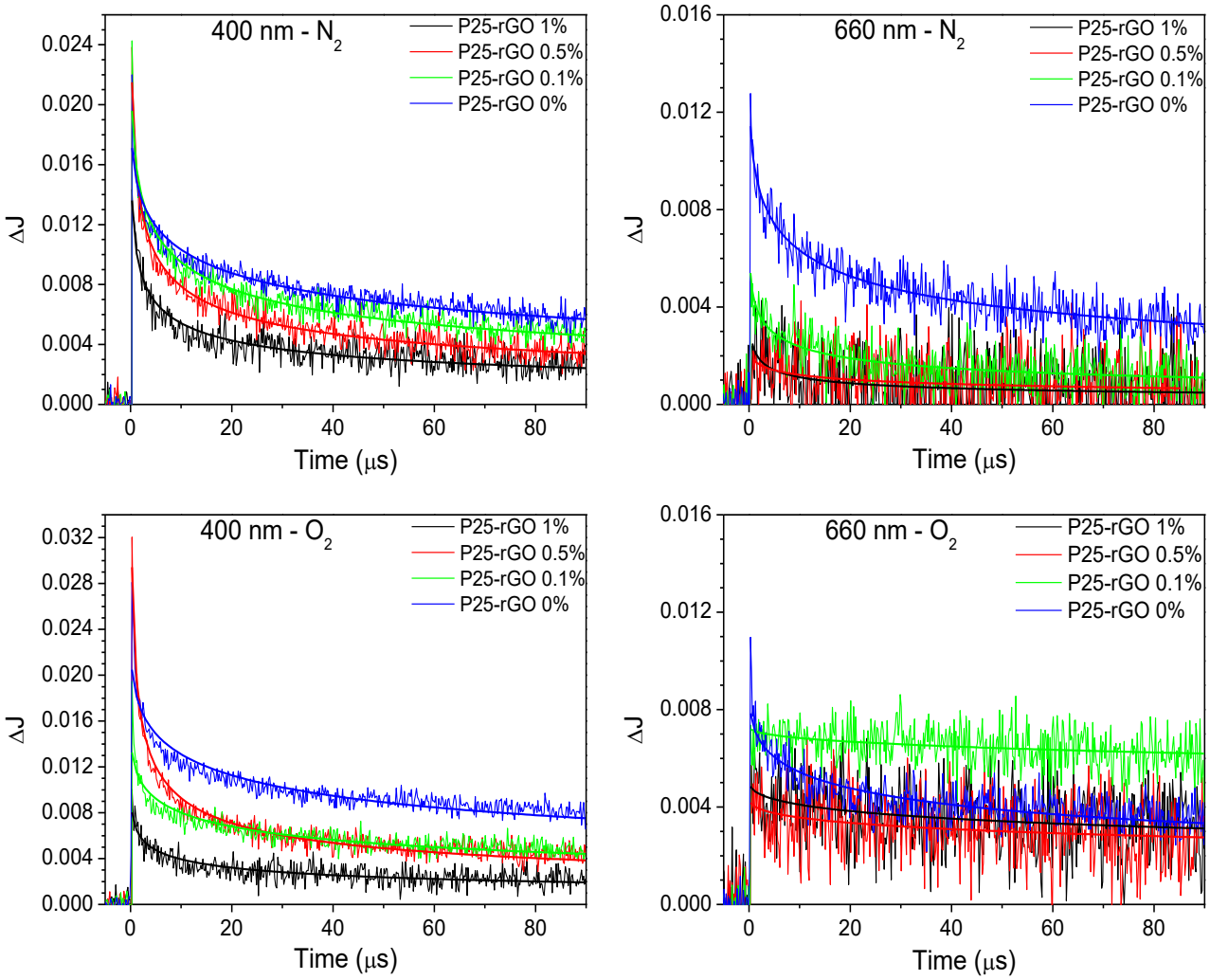


**Figure 12. Time profiles of transient absorption at 400 nm and 660 nm of P25-rGO 0%, P25-rGO 0.1%, P25-rGO 0.5% and P25-rGO 1% under a $N_2$ and $O_2$ atmosphere.**

***Graphical Abstract**

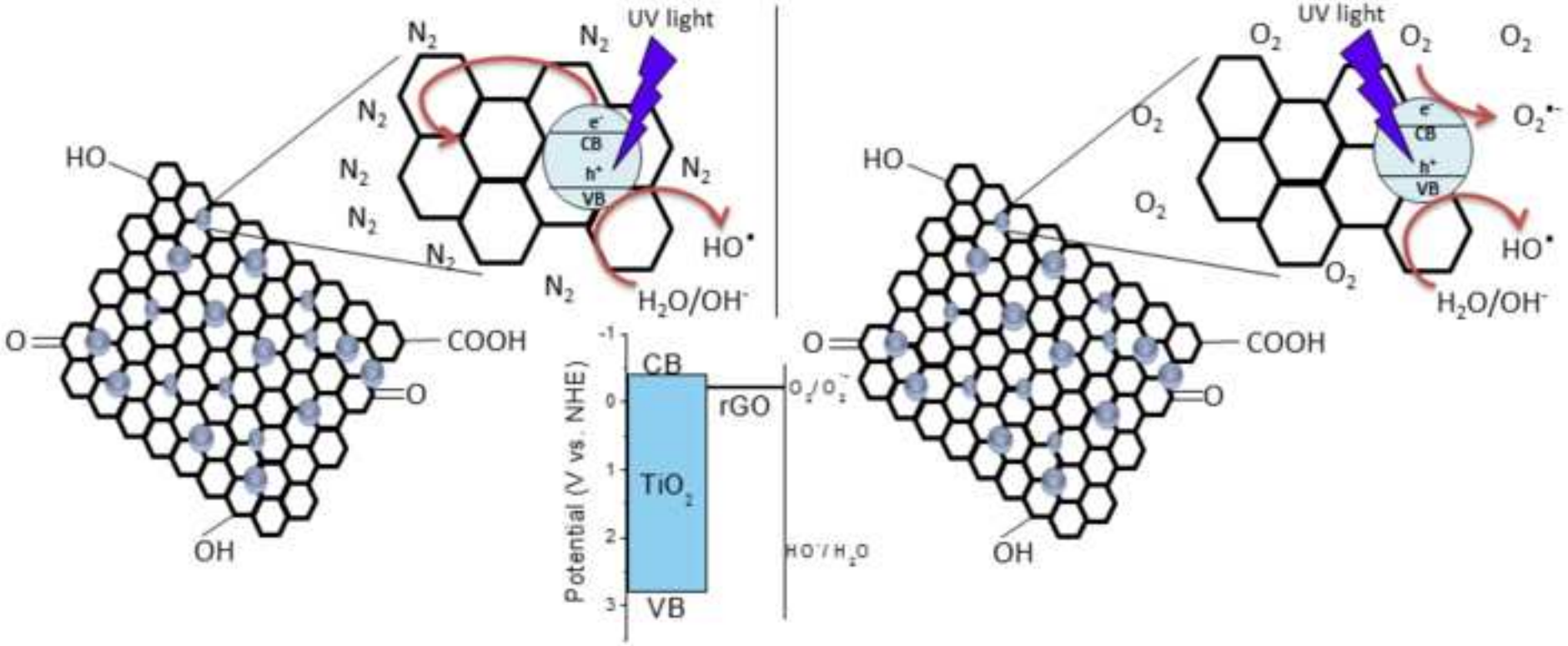

## Highlights

- rGO addition efficiently boosts charge transfer and therefore photocurrent values
- Lower charge transfer resistance found in $TiO_2$-rGO led to higher $O_2$ reduction current
- Low differences in $O_2^{\bullet-}$ and $HO^{\bullet}$ were detected in the $O_2$ saturated suspensions
- The role of rGO as an electron acceptor is less significant in $O_2$ atmosphere

**Supplementary Material**

**Click here to download Supplementary Material: Supplementary information_Sep 2018.docx**